



Extreme water levels along the central Red Sea coast of Saudi Arabia: processes and frequency analysis

Item Type	Article
Authors	Antony, Charls;Langodan, Sabique;Dasari, Hari Prasad;Knio, Omar;Hoteit, Ibrahim
Citation	Antony, C., Langodan, S., Dasari, H. P., Knio, O., & Hoteit, I. (2020). Extreme water levels along the central Red Sea coast of Saudi Arabia: processes and frequency analysis. Natural Hazards. doi:10.1007/s11069-020-04377-y
Eprint version	Post-print
DOI	10.1007/s11069-020-04377-y
Publisher	Springer Nature
Journal	Natural Hazards
Rights	Archived with thanks to Natural Hazards
Download date	2024-03-13 07:36:15
Link to Item	http://hdl.handle.net/10754/665688

1 **Extreme water levels along the central Red Sea coast of Saudi Arabia:**
2 **Processes and frequency analysis**

3 Charls Antony, Sabique Langodan, Hari Prasad Dasari, Omar Knio, Ibrahim Hoteit*

4 Physical Science and Engineering Division, King Abdullah University of Science and
5 Technology, Thuwal, Saudi Arabia

6
7 ***Corresponding author:** Prof. Ibrahim Hoteit, King Abdullah University of Science and
8 Technology (KAUST), Physical Science and Engineering Division, Thuwal 23955-6900, Saudi
9 Arabia. E-mail: ibrahim.hoteit@kaust.edu.sa

Abstract

Knowledge about extreme water levels is essential for efficient planning and design of coastal infrastructure. This study uses a high-resolution (~ 60 m) coupled ADvanced CIRCulation+ Simulating WAVes Nearshore (ADCIRC+SWAN) modeling system to estimate extreme water levels in the coastal waters of King Abdullah Economic City (KAEC), Saudi Arabia, located on the central eastern coast of the Red Sea. High spatial- (5-km) and temporal- (hourly) resolution meteorological fields are generated to drive the model, along with open ocean tides. The characteristics of extreme water levels in the region are subsequently described based on the validated model simulations. The central Red Sea is characterized by a low-tidal regime and meteorological events contribute significantly to total water levels: meteorological surges cause water level increases of up to 75 cm inside the KAEC lagoon. An extreme value analysis based on annual maxima of hindcast water level data is conducted and the results suggest that the inferred 100-year water levels are about 80 cm inside the KAEC lagoon. It is also shown that projected sea level rise would reduce the average recurrence intervals of extreme water levels along the KAEC coastline.

Keywords: Red Sea; Saudi Arabia; King Abdullah Economic City; Extreme sea levels; Meteorological surges; Return periods.

1. Introduction

Knowledge about extreme water level characteristics and their impacts is crucial to minimize associated risks and develop effective plans and mitigation measures. Determining the probability of extreme events is also necessary for coastal application aspects, and conducting a frequency analysis of extreme water levels is useful when designing various coastal structures (McInnes et al., 2003). In this respect, long-term tide gauge data can be analyzed to estimate the risk of flooding using various statistical analysis techniques (Haigh et al., 2010). However, long-term tide gauge data for the Red Sea are limited, and advanced numerical model outputs are the main source of information to obtain long-term water level data.

The Red Sea is an elongated semi-enclosed marginal sea in the Indian Ocean (Figure 1). It connects to the Gulf of Aden in the south via a narrow strait called Bab-el-Mandeb, which has a width of 25 km and maximum depth of only 137 m at the Hanish Sill. In the north, the basin branches into two smaller Gulfs; the Gulf of Suez and Gulf of Aqaba. Several studies on surface winds over the Red Sea have been conducted over the past (Langodan et al., 2017; Viswanadhapalli et al., 2017), and four major systems controlling the wind patterns over the sea have been suggested; North-northwest (NNW) winds, South-southeast (SSE) winds, Tokar Gap wind jet and mountain-gap winds in the northern Red Sea. NNW winds blow during May–October over the entire Red Sea, and the remnants of storms over the eastern Mediterranean often promote wind speeds of about 15 m/s. During the winter months, and particularly between November and April, SSE winds blow over the southern Red Sea (below 18°N). These winds are an extension of northeasterly monsoon winds blowing over the Arabian Sea, and they are channeled into the southern Red Sea by the orography surrounding the Gulf of Aden and the southern Red Sea. The existence of both NNW winds in the north and SSE winds in the south creates a convergence zone

1 at around 18°N (Langodan et al., 2015). In addition to these two prominent wind systems, there
2 are two other small-scale systems in the Red Sea that result from intense flows through the narrow
3 valleys cutting across the mountain ridges bordering the sea. The most prominent is the Tokar Gap
4 wind jet, which is located at approximately 18 °N off the African coast. In the northern Red Sea,
5 the mountain-gap winds usually originate from the Arabian subcontinent and gush westward.

6 Semidiurnal tides dominate in the Red Sea and the tidal amplitudes are small owing to the
7 restricted connection to the larger ocean (Pugh et al., 2019). The maximum spring tidal range is
8 about 1 m in the northern most parts of the Gulf of Suez and near Perim Island in the southern Red
9 Sea (Pugh et al. 2019). However, in the central Red Sea, the tidal range drops to 0.2 m where the
10 tidal amphidrome is present (Madah et al., 2015; Gharbi et al., 2018). Even so, the tidal phase has
11 significant impact on total water level as a storm event occurring during a high tide causes higher
12 inundation than the same event during a low tide (Antony et al., 2020). In a small tidal regime such
13 as that of the Red Sea, water level changes due to meteorological forces can be significant. The
14 meteorological surges are caused by two main processes: variations of wind and atmospheric
15 pressure (Pugh and Woodworth, 2014). A change in atmospheric pressure causes the water level
16 to change: there is a rise in the water level with a decrease in pressure, and the opposite occurs
17 when the pressure increases (an approximate quantification of the change in water level is 1 cm
18 for a 1 mb change in pressure). Wind plays a major role in generating surges in coastal waters
19 (Murty and El-Sabh, 1992). In particular, strong winds in the onshore direction cause water to pile
20 up toward the coast, and generate surges and coastal floods. Local geographical features of coastal
21 regions, as in the shallow waters and funnel-shaped bays, further enhance surges. The study by
22 Churchill et al. (2018) using bottom pressure and altimeter data reported that weather-band (~4–
23 30 days) sea level variations in the Red Sea exhibit a uniform basin-wide nature. They also reported

1 that the amplitude of weather-band signals is higher than those of tidal and seasonal sea levels, and
2 that these signals are associated with winds over the southern Red Sea.

3 Wave setup refers to the increase in water level due to the presence of breaking waves
4 (Nielsen, 1988) and it has been shown to be an important contributor to extreme water levels during
5 storm events (Murty et al., 2014; Samiksha et al., 2017; Krien et al., 2017). Previous studies have
6 reported that wave setup can be significant over fringing reefs with a steep fore reef (e.g., Vetter
7 et al., 2010). Wave setup can be a potential contributor to the extremes in the Red Sea as many of
8 its coastal areas are characterized by fringing reefs.

9 The monthly mean sea level is higher in winter than summer, and this is mainly driven by
10 the winds over the Red Sea (Safianos and Johns, 2001). The weather-band sea level fluctuations
11 are frequent during winter months (Churchill et al., 2018) and high background sea level during
12 the same period can elevate the total sea levels. Variations in sea level do occur on interannual
13 timescales in relation to the regional climate phenomena such as the El Niño Southern Oscillation,
14 the Indian Ocean Dipole, etc., which also contribute to the extreme sea level variability (Antony
15 et al., 2016). Such variations in the sea level are reported in the case of the Red Sea (Manasrah et
16 al., 2009; Alawad et al., 2019; Abdulla and Al-Subhi, 2020). In addition, mean sea level rise from
17 global climate change is also a pressing concern for coastal regions. Long-term tide gauge
18 measurements indicate a global mean sea level rise of about 1.7 mm/yr over the last century and
19 an increased mean sea level rise of 3.2 mm/yr over the past two decades (Church et al., 2013).
20 Previous studies suggested that the primary cause of the increase in extreme sea levels is the rising
21 mean sea level (e.g., Woodworth and Blackman, 2004). The Red Sea is not exempt from rising sea
22 levels (Pugh and Abualnaja, 2015) and associated impacts (El-Raey, 2010). Another potential
23 factor that can influence the extremes sea levels is the mesoscale eddies (Firing and Merrifield,

2004). The Red Sea is characterized by mesoscale eddies lasting several weeks (Zhan et al., 2014). These eddies also elevate the coastal sea level occasionally (Churchill et al., 2018).

To the best of our knowledge, extreme water levels have not been investigated yet in the Red Sea. Here we analyze the extreme water level characteristics in the vicinity of King Abdullah Economic City (KAEC) in the central eastern Red Sea (Figure 1). KAEC (<https://www.kaec.net>) is located in the western Kingdom of Saudi Arabia (KSA), approximately 100 km north of Jeddah. The developing city covers an area of 181 km², has a coastline of 40 km, and is designed to accommodate two million people (Moser et al., 2015). It comprises King Abdullah Port, which is the largest port on the Red Sea, the Coastal Communities residential districts, the Haramain Railway district, and the Industrial Valley. KAEC is surrounded by numerous fringing and offshore coral reef systems on the ocean side, and includes a shallow lagoon that extends about 9 km from its entrance to the inner most point at the southern end (Figure 1c).

We investigate the characteristics of extreme water levels in the near-shore regions of KAEC based on high-resolution long-term hindcast data generated using a state-of-the-art coupled tide-surge-wave modeling system. Determining water levels with certain return periods (average recurrence intervals) is a widely used and an effective method for assessing the potential risk of coastal hazards and their impact on the design of coastal and offshore facilities and planning harbor operations. The potential risk of extreme water levels occurring throughout the region is also assessed by estimating the return periods of extreme water levels. The remainder of this paper is organized as follows: Section 2 describes the data and methodology, including the coupled modeling system, observational data, and evaluation methods; Section 3 presents the results and discussion; and Section 4 summarizes our main findings.

2. Data and methods

2.1 Modeling framework

The water levels along the KAEC coastline are simulated using a coupled tide-surge-wave modeling system configured on an unstructured grid. The coupled system includes the two-dimensional (2D) depth-averaged ADCIRC model (version 50.99.13, Luetlich et al., 1992; Luetlich and Westerink, 2004) to simulate meteorological surge and tides, and SWAN (version 40.91, Booij et al., 1999) to simulate ocean waves. Coupling ADCIRC with SWAN provides the added advantage of considering the contribution of wind waves to the total water level, in addition to wind, pressure, and tide-induced changes. Although three-dimensional (3D) hydrodynamic models are now widely used, implementing them at coastal scales resolutions and given the considerable run times for over long-term periods remain computationally very demanding. 2D models have the advantage of providing reliable water level simulation at reasonable computational cost. The model domain covers the entire Red Sea and the Gulf of Aden, and the open boundary extends into the Arabian Sea to include open ocean tides (Figure 1a). High resolution light detection and ranging (LiDAR) is used to estimate the bathymetry of coastal waters (up to a depth of 30 m) in the vicinity of KAEC. This dataset is combined with data from the General Bathymetric Chart of the Oceans (available at a resolution of 30 arc seconds) for the rest of the domain. The LiDAR survey was conducted in 2009 and has an accuracy of ± 10 cm.

An unstructured triangular mesh of 92,215 nodes (180,695 elements) is implemented in the study, and the mesh is designed with a fine resolution near the coast and a coarse resolution in the deep water. The model grid resolution is about 60 m near the KAEC coastline, 5 km within the Red Sea, and increasing to 60 km near the open boundary. The boundary tides are obtained from a global model, Finite Element Solution 2012 (Carrère et al., 2012), and the major tidal

constituents (M_2 , S_2 , K_2 , N_2 , K_1 , O_1 , P_1 , and Q_1) are prescribed at the open boundary. The bottom stress formulation in the model is quadratic in nature, with friction coefficient of 0.0025. The horizontal eddy viscosity is set to $5 \text{ m}^2/\text{s}$. ADCIRC and SWAN use the same unstructured mesh, and the coupling mechanism involves the transfer of wave radiation stress gradients from SWAN to ADCIRC, and water levels and currents from ADCIRC to SWAN (Dietrich et al., 2011). ADCIRC+SWAN simulations are conducted using atmospheric and tidal forcing in blocks of one month periods with an additional five days ramp-up period for a total of 31 years (1985–2015). The outputs are stored at hourly intervals for further analysis.

2.2 Atmospheric forcing

The coupled model is forced with hourly wind components (u and v at a height of 10 m) and mean seal level pressure extracted from the Red Sea atmospheric reanalysis (Dasari et al., 2019a, 2019b; Viswanadhapalli et al., 2017), generated using the Advanced Research Weather Research and Forecasting model (WRF, Skamarock et al., 2008), at a 5 km horizontal resolution and available over a 31 years period between 1985 and 2015. The WRF model is implemented with two, two-way nested domains with horizontal resolutions of 15 and 5 km, respectively, and 51 vertical levels, and it is initialized using the European Centre for Medium-Range Weather Forecasts (ECMWF) Interim reanalysis data (ERA-I) available at a horizontal resolution of 0.75° (Dee et al., 2011). All available satellite and in-situ observations in the region are assimilated into WRF using the consecutive re-initialization method as described by Viswanadhapalli et al. (2017) and Langodan et al. (2014, 2016), where daily initialized simulations are conducted for a 36-h period starting at 12:00 UTC each day; the first 12-h period is neglected as the spin up time, and the remaining 24-h data are combined to generate long-term (1985–2015) high-resolution atmospheric reanalysis. This data was widely used in several Red Sea studies and was extensively validated

with the in-situ and remote sensing observations (e.g., Viswanadhapalli et al., 2017, 2019a, 2019b; Dasari et al., 2019a, 2019b).

2.3 Tide gauge data

The Red Sea is a data-scarce region, and only a limited number of tide gauge observations are available to validate the model simulations. We use observations collected during the oceanographic and meteorological measurement program conducted by Fugro Global Environmental and Ocean Sciences Ltd during December 2006 to February 2007 in the coastal waters of KAEC. Measurements are taken at 10 m interval at five locations shown in Figure 1c.

The tidal constituents are determined from one month-data (21 January 2007 to 20 February 2007) obtained at these five locations and they are used for site-specific validation of the modeled tides. We also use tide gauge data collected at hourly interval at Rabigh (Figure 1b) to validate the modeled total water levels. The data are provided by the Saudi General Commission for Survey for a period from 1 January 2011 to 31 December 2013. 100% data are available at all locations and observations are quality controlled during post-processing to identify and remove anomalous values before comparison.

2.4 Validation methodology

The agreement between the observed and the corresponding modeled tidal constituent, derived through a harmonic analysis, is evaluated based on the modulus of the complex difference (Mayet et al., 2013):

$$|\Delta z| = |A_o e^{i\phi_o} - A_m e^{i\phi_m}|, \quad (1)$$

where A_o , A_m , and ϕ_o , ϕ_m are the observed and modeled amplitudes and phases, respectively.

1 The total error for all constituents at one site is given as:

$$2 \quad \sigma_s = \sqrt{\frac{1}{2} \sum_{N_{\text{constituent}}} |\Delta z|^2}. \quad (2)$$

3 The total water level time series from the observations and model outputs are compared by
4 computing the root mean square error (RMSE) and correlation coefficient (r).

5 **2.5 Extreme value analysis**

6 Different methods have been proposed to estimate the probability of extreme water levels (such as
7 Unnikrishnan et al., 2004; Haigh et al., 2010; Arns et al., 2013), and there is no universal method
8 for conducting an extreme value analysis (EVA) (Haigh et al., 2010). The most common method
9 is based on annual maxima of water levels that are fitted a Gumbel distribution or Generalized
10 Extreme Value (GEV) distribution (Kirezci et al., 2020). One limitation of this annual maxima
11 approach is that it uses only one value per year. The data are therefore not fully used in the analysis
12 as several other extremes could occur within a year that are higher than other years maxima. Two
13 other methods were introduced to overcome this issue; the peak over threshold (POT) method and
14 the r-largest method. In the POT method, extremes above a specified threshold are fitted to the
15 generalized pareto distribution whereas in the second method r-largest values per year are
16 considered and fitted to the GEV distribution. Though these two methods include larger number
17 of events per year, there is no consent in the community about one approach over another. The
18 annual maxima method was indeed suggested to provide reliable estimates of probability curves
19 when 30 or more years of data are used (Bernier et al., 2007; Wahl et al., 2017).

In this study, we conducted an EVA based on 31-year data set using the annual maxima method and the GEV distribution. This method was selected as it performed better than the other tested methods with our data set.

The GEV distribution function is defined as:

$$G(z) = \exp \left\{ - \left[1 + \xi \left(\frac{z - \mu}{\sigma} \right) \right]^{\frac{-1}{\xi}} \right\}, \quad (3)$$

where σ is a scale parameter, μ is the location parameter, ξ is the shape parameter, and the annual maximum water levels are z .

The return level Z_m , corresponding to a return period m (say, 50-yr), can be determined as:

$$Z_m = \mu - \frac{\sigma}{\xi} \left\{ 1 - \left[-\log \left(1 - \frac{1}{m} \right) \right]^{-\xi} \right\}. \quad (4)$$

The EVA is conducted using the extRemes package (Gilleland and Katz, 2016) implemented in the statistical language, R (<http://www.r-project.org/>). The parameters of the distributions are estimated using the maximum likelihood estimation method, and the upper and lower 95 % confidence limits are obtained using the Delta method (Gilleland and Katz, 2016). A fundamental assumption when conducting an EVA is that time series are stationary and extreme events are independent (Coles, 2001; Arns et al., 2013). However, environmental variables often depend on past values and their statistical properties often vary over time. The use of the annual maxima can be justified as the extreme events are independent, we further account for stationarity by applying a linear detrending to the time series prior to conducting the EVA. The annual maximum water levels derived from 31-yr hourly model simulations are used to estimate the return water levels for different return periods up to 100-yr. Therefore, the return period estimation did not exceed 3–4 times the length of the underlying time series, which is the recommended limit in the literature (e.g., Bernier et al., 2007; Pugh and Woodworth, 2014).

Annual maximum water levels are assigned a probability using the Weibull's plotting position formula, and return periods are calculated as:

$$T_i = \frac{n+1}{i}, \quad (5)$$

where T_i is the return period corresponding to the i th annual maximum water level, i is the ranking of the water level data from high to low; and n is the total number of years.

3. Model validation

3.1 Tides

The tidal constituents from five stations (Figure 1c) near the KAEC coastline are compared against those obtained from the model. A harmonic analysis of water level data spanning one month (21 January 2007 to 20 February 2007) is used to derive the tidal constituents. A visual assessment of the scatter diagrams of observed and modeled tidal constituents (Figure 2) shows that the amplitudes of the constituents are underestimated (up to 17% for M_2) by the model, and the phases of the modeled and observed constituents are in good agreement (within 10% error). The estimated errors based on Equations 1 and 2 are presented in Table 1, where the error values reveal that σ_s is low (of about 0.96 cm) at Station 1 and higher (of about 1.8 cm) at Station 5.

3.2. Water levels

We use data collected over three years using a tide gauge located at the Port of Rabigh (~20 km north of KAEC) to validate the simulated total water levels. As shown in Figure 3, the model is generally in good agreement with the observations with RMSE and r values of 10.77 cm and 0.83, respectively. There are however few instances where the model fails to simulate the observed minimum and maximum in the data time series. Because we used a 2D model, changes in water

level due to baroclinic effects are not accounted for. A methodology based on oceanic reanalysis data is adopted to improve the simulated water levels is discussed in the next section.

4. Improving simulated water level data

The comparison between 2D model and observation suggested noticeable disagreement between the two on seasonal time scales. To improve the 2D model water levels we added monthly mean sea levels simulated by a 3D model to adjust the seasonal differences following the procedure suggested by Zhai et al. (2019). We used an ocean reanalysis product of the ECMWF, ORAS5 (Zuo et al., 2019), that was generated using the Nucleus for European Modeling of the Ocean (NEMO). ORAS5 data are available monthly at 0.25° resolution. The 2D model adjustment is applied as follows; (i) the difference between monthly mean sea level of the ORAS5 data and 2D model is first computed, (ii) the computed difference is then interpolated to hourly intervals and, (iii) final adjusted data is then obtained by adding the hourly 2D model data and hourly differences. Basically, the missing baroclinic sea level on monthly and higher time scales was added to the 2D model. Since pressure forcing is not used in the generation of reanalysis data, the monthly mean sea levels of the 2D model are computed from a wind-only forced run for consistency. The result of this adjustment is shown in Figure 3, showing a noticeably better agreement between the observed and modeled data. The error statistics (Figure 3) have improved from 10.77 cm to 8.75 cm for RMSE and from 0.83 to 0.88 for correlation coefficient r . There is still however few disagreements between the model and observation over periods shorter than a month, as baroclinic effect within this time scale are not accounted for. The main goal of this study is the calculation of return levels, and from this perspective a good agreement of the data sets in terms of quantile-quantile (Q-q) plots is recommended (Calafat et al., 2014). Figure 4 shows the Q-q plot at Rabigh. The deviation between the model and observed distributions has considerably reduced after the

model adjustment. The modeled extreme high water levels are now in good agreement with the observations (differences are within 5 cm). This provides us confidence in analyzing the extreme water level along the KAEC coast based on the adjusted model results.

5. Results and discussion

5.1 Characteristics of extreme water levels

We first analyze the occurrence of surge events along the KAEC coastline. Figure 5a shows the surge time series at a location in the central Red Sea near KAEC, together with surge time series from locations in the northern and southern Red Sea (see Figure 6a for locations). The plot indicates that the surge is nearly uniform throughout the Red Sea. Figure 5b, c, and d show the pressure and zonal and meridional components of surface wind, respectively, at the same locations shown in Figure 5a. A visual inspection of these time series reveals that the patterns of surges tend to be similar to the meridional component of winds over the southern Red Sea. This is confirmed by a correlation analysis between long-term (1980–2015) time series of meteorological parameters at different locations and surges in KAEC (Table2). The time series of surge at KAEC is strongly correlated (>0.60) with the wind components over the southern Red Sea, whereas the wind components at KAEC and the northern Red Sea exhibit weak correlations (<0.2) with the local surge.

This study focuses on a small region within the Red Sea, and we are therefore interested in determining whether any local meteorological features occur during the surge events near KAEC, which can locally modulate the basin-wide signals. In this respect, we show snapshots of the metrological fields during certain extreme high and low water levels in Figure 6. High water level events are generally characterized by strong SSE winds (Figure 6c) over the southern Red Sea, whereas weakening or reversal of SSE wind (Figure 6a and b) over the southern Red Sea is

1 accompanied by low water level events. Convergence of NNW and SSE winds are evident in
2 Figure 6c, which creates strong winds near KAEC. Such high winds can locally further enhance
3 the surge height, especially inside the shallow KAEC lagoon.

4 We also analyzed the spatial patterns of surge and maximum water levels. Figure 7 presents
5 spatial maps of maximum water level, meteorological surge, and wave setup at the coastal waters
6 of KAEC. A maximum water level of about 75 cm is estimated inside the KAEC lagoon, and this
7 value is slightly lower along the open coast (60–65cm). In the near-coastal regions, maximum
8 water levels are related to the surge contribution, with Figure 7b showing that the surge component
9 reaches magnitude close to those of the maximum water levels. The surge increases from the open
10 coast to the inner regions of the lagoon. The KAEC lagoon is characterized by very shallow depths
11 and is a semi-enclosed environment these features, together with favorable wind conditions, can
12 amplify surge heights inside the lagoon.

13 Figure 8 presents time series of model-simulated tides, meteorological surge, wave setup,
14 and total water level at the three locations indicated in Figure 7b. The results reveal marked
15 seasonal patterns in meteorological surges and the resulting total water levels. Most of the surges
16 occur during the winter months (October–March), whereas lowest values of water levels occur in
17 the summer months (June–September). These occurrences are consistent with the wind patterns
18 over the southern Red Sea.

19 To assess the wave setup contributions to the water level along the KAEC coastline, we
20 compared the water level as resulting from wave coupled (tide-surge-wave) and uncoupled (tide-
21 surge) model simulations. The difference in water levels between coupled and uncoupled models
22 is attributed to the wave setup, and the corresponding spatial map of maximum wave setup for the

KAEC region is shown in Figure 7c. The results suggest that the wave setup is almost negligible near the lagoon entrance and inside the lagoon owing to the sheltered nature of the regions from wave breaking. However, the drastic transition in the bathymetry (from 30 m to less than 1 m) along the coastal areas of the northern part of KAEC results in significant wave setup that is typically about 5-10 cm (Figure 8a), but occasionally reaches up to 20 cm (Figure 7c). We also estimated the wave setup contributions to the extremes water levels over 99th percentile and found that the average contribution is less than 5%.

5.2 Statistics of extreme sea levels

Return levels of extreme high water levels along the KAEC coastline are estimated using the annual maximum water levels and the GEV distribution for various return periods, and the corresponding results are presented in Figure 9. Figures 9a, b, and c display the return level curves for three locations along the KAEC coastline, L1, L8, and L19, as indicated in Figure 9d. L1 and L8 are open coast locations, whereas L19 is located inside the lagoon, where the highest water level during the 31-yr study period is observed. The GEV distribution provides a good fit to the model-simulated data at L1 and L8. However, at L19, the fit generally follows the data up to 10-yr, before it diverges for higher (15- and 31-yr) return periods. The spatial patterns of the 50- and 100-yr return levels are shown in Figures 9e and f, respectively. The open coastal areas of KAEC exhibit small return levels compared to the shallow inner regions of the KAEC lagoon and the inferred 100-year water levels are about 80 cm inside the KAEC lagoon. As noted from the return level plots for L19 (Figure 9c), the return levels inside the lagoon are underestimated. The difference between the 31-yr maxima (Figure 9d) and corresponding return levels from GEV distribution is shown in Figure 9g; the figure indicates that the largest differences (up to 6 cm) are

found inside the KAEC lagoon and the differences for the remaining coastline are mostly below 4 cm.

In addition to determining return levels under present climate conditions, we also assessed the impact of present rate of sea level rise on extreme water level statistics by year 2050. The study by Alawad et al. (2019) estimated the mean sea level rise trend in the Red Sea at 2.8 mm/yr over the period 1993-2017, which is lower than the global trend (3.2 mm/yr). At this rate the Red Sea would experience approximately 0.1 m increase in sea level by 2050. The mean sea level rise influence on the return level is examined by adding the 2050 0.1 m level rise to the return levels obtained based on the current climate conditions in the Red Sea. A similar approach to account for the influence of sea level rise on the extreme sea level frequency has been applied by McInnes et al. (2003), Tebaldi et al. (2012) and Rasmussen et al. (2018). The resulting return level curve for the future climate scenario for 2050 at location L19 is presented in Figure 10. A comparison of the current and future climate curves shows that the estimated mean sea level rise reduces the average recurrence interval of present 50- and 100-yr levels to 10- and 20-yr by 2050.

6. Summary and conclusions

This study investigated the extreme water levels in the coastal waters of KAEC, KSA, situated on the central east coast of the Red Sea. A high-resolution (~60 m) tide-surge-wave coupled modeling system (ADCIRC+SWAN) forced with meteorological fields from high-resolution (5km) Red Sea regional reanalysis data was implemented and its outputs were analyzed. Meteorological surges were found to reach as high as 65 cm in the open coastal waters of KAEC, whereas inside the KAEC lagoon, shallowness, favorable geometry, and winds lead to slightly higher surges (about 75 cm). Seasonally, meteorological surges are prominent during winter (October-March). We observed water levels up to 20 cm resulting from the wave setup in the northern coastal waters of

KAEC, whereas this was negligible inside the lagoon. Furthermore, return periods of extreme high water levels along the KAEC coastline were estimated and 100-yr return levels up to 80 cm were found inside the KAEC lagoon. The impact of climate change on extreme high water levels along the KAEC coastline through mean sea level rise indicated that present 50- and 100-yr events becoming future (2050) 10- and 20-yr events, respectively.

The central Red Sea is known to be a low-tidal regime; therefore, non-tidal water level changes are very important. Abnormal water levels during surge events can aggravate wave actions and may cause important erosions along the coast.

Acknowledgments

This research was supported by funds from the Office of Sponsored Research (OSR) under the virtual Red Sea Initiative (Grant #REP/1/3268-01-01) at King Abdullah University of Science and Technology (KAUST). The study made use of the Supercomputing Laboratory resources at KAUST. Data used in this study can be made available on request. Graphs and maps were drawn using GMT (Generic Mapping Tools, Wessel et al., 2013) and FigureGen (Dietrich et al., 2013). The authors would like to thank the ADCIRC+SWAN model developers for making the model freely available.

Compliance with Ethical Standards

Conflict of interest: The authors have no conflicts of interest to declare that are relevant to the content of this article.

References

Abdulla, C.P. and Al-Subhi, A.M., 2020. Sea Level Variability in the Red Sea: A Persistent East–West Pattern. *Remote Sensing*, 12(13), p.2090.

- 1 Alawad, K.A., Al-Subhi, A.M., Alsaafani, M.A., Alraddadi, T.M., Ionita, M. and Lohmann, G.,
2 2019. Large-Scale Mode Impacts on the Sea Level over the Red Sea and Gulf of
3 Aden. *Remote Sensing*, 11(19), p.2224.
- 4 Antony, C., Unnikrishnan, A.S., Krien, Y., Murty, P.L.N., Samiksha, S.V. and Islam, A.K.M.S.,
5 2020. Tide–surge interaction at the head of the Bay of Bengal during Cyclone
6 Aila. *Regional Studies in Marine Science*, 35, p.101133.
- 7 Antony, C., Unnikrishnan, A.S. and Woodworth, P.L., 2016. Evolution of extreme high waters
8 along the east coast of India and at the head of the Bay of Bengal. *Global and planetary
9 change*, 140, pp.59-67.
- 10 Arns, A., Wahl, T., Haigh, I.D., Jensen, J. and Pattiaratchi, C., 2013. Estimating extreme water
11 level probabilities: A comparison of the direct methods and recommendations for best
12 practise. *Coastal Engineering*, 81, pp.51-66.
- 13 Bernier, N.B., Thompson, K.R., Ou, J. and Ritchie, H., 2007. Mapping the return periods of
14 extreme sea levels: allowing for short sea level records, seasonality, and climate
15 change. *Global and Planetary Change*, 57(1-2), pp.139-150.
- 16 Booij, N.R.R.C., Ris, R.C. and Holthuijsen, L.H., 1999. A third-generation wave model for coastal
17 regions: 1. Model description and validation. *Journal of geophysical research:
18 Oceans*, 104(C4), pp.7649-7666.
- 19 Calafat, F.M., Avgoustoglou, E., Jordá, G., Flocas, H., Zodiatis, G., Tsimplis, M.N. and
20 Kouroutzoglou, J., 2014. The ability of a barotropic model to simulate sea level extremes
21 of meteorological origin in the Mediterranean Sea, including those caused by explosive
22 cyclones. *Journal of Geophysical Research: Oceans*, 119(11), pp.7840-7853.
- 23 Carrère, L., Lyard, F., Cancet, M., Guillot, A. and Roblou, L., 2012, September. FES 2012: a new
24 global tidal model taking advantage of nearly 20 years of altimetry. In *20 Years of Progress
25 in Radar Altimetry* (Vol. 710).
- 26 Church, J.A., Clark, P.U., Cazenave, A., Gregory, J.M., Jevrejeva, S., Levermann, A., Merrifield,
27 M.A., Milne, G.A., Nerem, R.S., Nunn, P.D., Payne, A.J., Pfeffer, W.T., Stammer, D.,
28 Unnikrishnan, A.S., 2013. In: Stocker, T.F., Qin, D., Plattner, G.-K., Tignor, M., Allen,
29 S.K., Boschung, J., Nauels, A., Xia, Y., V., Bex, Midgley, P.M.(Eds.), *Sea Level Change*.
30 In: *Climate Change 2013: The Physical Science Basis. Contribution of Working Group I to
31 the Fifth Assessment Report of the Intergovernmental Panel on Climate Change*.
32 Cambridge University Press, Cambridge, United Kingdom and New York, NY, USA,
33 pp.1137-1216.
- 34 Churchill, J.H., Abualnaja, Y., Limeburner, R. and Nellayaputhenpeedika, M., 2018. The
35 dynamics of weather-band sea level variations in the Red Sea. *Regional studies in marine
36 science*, 24, pp.336-342.
- 37 Coles, S., 2001. *An introduction to statistical modeling of extreme values* (Vol. 208, p. 208).
38 London: Springer.
- 39 Dasari, H.P., Srinivas, D., Langodan, S., Raju, A., Yesubabu, V., Ravikumar, K. and Hoteit, I.,
40 2019: Assessment of solar radiation resources and its variability over Arabian Peninsula.
41 *Applied Energy*. 248, 354-371.
- 42 Dasari, H.P., Desamsetti, S., Langodan, S., Attada, R., Kunchala, R. K., Viswanadhapalli, Y.,
43 Knio, O., and Hoteit, I., 2019. High-resolution assessment of solar energy resources over
44 the Arabian Peninsula. *Applied Energy*, 248, 354-371

- 1 Dee, D.P. and co-authors, 2011. The ERA-Interim reanalysis: configuration and performance of
2 the data assimilation system. *Q. J. R. Meteorol. Soc.*137:553–597.doi: 10.1002/qj.828.
- 3 Dietrich, J.C., Dawson, C.N., Proft, J.M., Howard, M.T., Wells, G., Fleming, J.G., Luettich, R.A.,
4 Westerink, J.J., Cobell, Z., Vitse, M. and Lander, H., 2013. Real-time forecasting and
5 visualization of hurricane waves and storm surge using SWAN+ ADCIRC and FigureGen.
6 In *Computational challenges in the geosciences* (pp. 49-70). Springer, New York, NY.
- 7 Dietrich, J.C., Zijlema, M., Westerink, J.J., Holthuijsen, L.H., Dawson, C., Luettich Jr, R.A.,
8 Jensen, R.E., Smith, J.M., Stelling, G.S. and Stone, G.W., 2011. Modeling hurricane waves
9 and storm surge using integrally-coupled, scalable computations. *Coastal Engineering*,
10 58(1), pp.45-65.
- 11 El-Raey, M.,2010. Impact of sea level rise on the Arab Region. UNDP Regional Bureau for Arab
12 States (UNDP-RBAS), Cairo, Egypt
- 13 Firing, Y.L. and Merrifield, M.A., 2004. Extreme sea level events at Hawaii: Influence of
14 mesoscale eddies. *Geophysical Research Letters*, 31(24).
- 15 Gharbi, S.H., Albarakati, A.M., Alsaafani, M.A., Saheed, P.P. and Alraddadi, T.M., 2018.
16 Simulation of tidal hydrodynamics in the Red Sea using COHERENS model. *Regional*
17 *studies in marine science*, 22, pp.49-60.
- 18 Gilleland, E. and Katz, R.W., 2016. extRemes 2.0: an extreme value analysis package in R. *Journal*
19 *of Statistical Software*, 72(8), pp.1-39.
- 20 Haigh, I.D., Nicholls, R. and Wells, N., 2010. A comparison of the main methods for estimating
21 probabilities of extreme still water levels. *Coastal Engineering*, 57(9), pp.838-849.
- 22 Kirezci, E., Young, I.R., Ranasinghe, R., Muis, S., Nicholls, R.J., Lincke, D. and Hinkel, J., 2020.
23 Projections of global-scale extreme sea levels and resulting episodic coastal flooding over
24 the 21st Century. *Scientific reports*, 10(1), pp.1-12.
- 25 Krien, Y., Testut, L., Islam, A.K.M.S., Bertin, X., Durand, F., Mayet, C., Tazkia, A.R., Becker,
26 M., Calmant, S., Papa, F. and Ballu, V., 2017. Towards improved storm surge models in
27 the northern Bay of Bengal. *Continental Shelf Research*, 135, pp.58-73.
- 28 Langodan, S., Cavaleri, L., Vishwanadhapalli, Y., Pomaro, A., Bertotti, L. and Hoteit, I., 2017.
29 The climatology of the Red Sea–part 1: the wind. *International Journal of*
30 *Climatology*, 37(13), pp.4509-4517.
- 31 Langodan, S., Cavaleri, L., Viswanadhapalli, Y. and Hoteit, I., 2015. Wind-wave source functions
32 in opposing seas. *Journal of Geophysical Research: Oceans*, 120(10), pp.6751-6768.
- 33 Langodan, S., Cavaleri, L., Viswanadhapalli, Y. and Hoteit, I., 2014. The Red Sea: a natural
34 laboratory for wind and wave modeling. *J. Phys. Oceanogr.* 44, 3139–3159.
- 35 Langodan, S., Viswanadhapalli, Y., Dasari, H.P., Knio, O. and Hoteit, I., 2016. A high-
36 resolution assessment of wind and wave energy potentials in the Red Sea. *Applied*
37 *Energy*. 181:244–255.
- 38 Luettich, Jr, R. A., Westerink, J.J. and Scheffner, N.W., 1992. ADCIRC: An Advanced Three-
39 Dimensional Circulation Model for Shelves, Coasts, and Estuaries. Report 1. Theory and
40 Methodology of ADCIRC-2DDI and ADCIRC-3DL (No.CERC-TR-DRP-92-6).COASTAL
41 ENGINEERING RESEARCH CENTER VICKSBURG MS.

- 1 Luetlich, R.A. and Westerink, J.J., 2004: Formulation and numerical implementation of the 2D/3D
2 ADCIRC finite element model version 44.XX. 74 pp. [Available online at
3 https://adcirc.org/files/2018/11/adcirc_theory_2004_12_08.pdf].
- 4 Madah, F., Mayerle, R., Bruss, G. and Bento, J., 2015. Characteristics of tides in the Red Sea
5 region, a numerical model study. *Open Journal of Marine Science*, 5(02), p.193.
- 6 Manasrah, R., Hasanean, H.M. and Al-Rousan, S., 2009. Spatial and seasonal variations of sea
7 level in the Red Sea, 1958–2001. *Ocean Science Journal*, 44(3), pp.145-159.
- 8 Mayet, C., Testut, L., Legresy, B., Lescarmontier, L. and Lyard, F., 2013. High-resolution
9 barotropic modeling and the calving of the Mertz Glacier, East Antarctica. *Journal of*
10 *Geophysical Research: Oceans*, 118(10), pp.5267-5279.
- 11 McInnes, K.L., Walsh, K.J.E., Hubbert, G.D. and Beer, T., 2003. Impact of sea-level rise and storm
12 surges on a coastal community. *Natural Hazards*, 30(2), pp.187-207.
- 13 Moser, S., Swain, M. and Alkhabbaz, M.H., 2015. King Abdullah economic city: Engineering
14 Saudi Arabia's post-oil future. *Cities*, 45, pp.71-80.
- 15 Murty, P.L.N., Sandhya, K.G., Bhaskaran, P.K., Jose, F., Gayathri, R., Nair, T.B., Kumar, T.S.
16 and Shenoi, S.S.C., 2014. A coupled hydrodynamic modeling system for PHAILIN
17 cyclone in the Bay of Bengal. *Coastal Engineering*, 93, pp.71-81.
- 18 Murty, T.S. and El-Sabh, M.I., 1992. Mitigating the effects of storm surges generated by tropical
19 cyclones: a proposal. *Natural Hazards*, 6(3), pp.251-273
- 20 Nielsen, P., 1988. Wave setup: A field study. *Journal of Geophysical Research: Oceans*, 93(C12),
21 pp.15643-15652.
- 22 Pugh, D. and Woodworth, P., 2014. Sea-level science: understanding tides, surges, tsunamis and
23 mean sea-level changes. Cambridge University Press.
- 24 Pugh, D.T. and Abualnaja, Y., 2015. Sea-level changes. In N.M.A. Rasul and I.C.F. Stewart
25 (eds.), *The Red Sea* (pp. 317-328). Springer, Berlin, Heidelberg.
- 26 Pugh, D.T., Abualnaja, Y. and Jarosz, E., 2019. The tides of the Red Sea. In *Oceanographic and*
27 *Biological Aspects of the Red Sea* (pp. 11-40). Springer, Cham.
- 28 Rasmussen, D.J., Bittermann, K., Buchanan, M.K., Kulp, S., Strauss, B.H., Kopp, R.E. and
29 Oppenheimer, M., 2018. Extreme sea level implications of 1.5 C, 2.0 C, and 2.5 C
30 temperature stabilization targets in the 21st and 22nd centuries. *Environmental Research*
31 *Letters*, 13(3), p.034040.
- 32 Samiksha, V., Vethamony, P., Antony, C., Bhaskaran, P. and Nair, B., 2017. Wave–current
33 interaction during Hudhud cyclone in the Bay of Bengal. *Natural Hazards and Earth*
34 *System Sciences*, 17(12), p.2059.
- 35 Skamarock, W.C., Klemp, J.B., Dadhia, J., Gill, D.O., Barker, D.M., Duda, M.G., Huang, X.Y.,
36 Wang, W. and Powers, J.G., 2008. A description of the Advanced Research WRF version
37 3, NCAR Tech. Note NCAR/TN-475-STR, 113 pp. Nat. Cent. For Atmos. Res, Boulder,
38 Colo.
- 39 Sofianos, S.S. and Johns, W.E., 2001. Wind induced sea level variability in the Red Sea.
40 *Geophysical research letters*, 28(16), pp.3175-3178.
- 41 Unnikrishnan, A.S., Sundar, D. and Blackman, D., 2004. Analysis of extreme sea level along the
42 east coast of India. *Journal of Geophysical Research: Oceans*, 109(C6).

- 1 Vetter, O., Becker, J.M., Merrifield, M.A., Pequignet, A.C., Aucan, J., Boc, S.J. and Pollock, C.E.,
2 2010. Wave setup over a Pacific Island fringing reef. *Journal of Geophysical Research:*
3 *Oceans*, 115(C12).
- 4 Viswanadhapalli, Y., Challa, V.S., Basha, G., Dasari, H.P., Ratnam, M.V., Langodan S. and
5 Hoteit, I., 2019a. A diagnostic study of extreme precipitation over Kerala during August
6 2018. *Atmospheric Science Letters*. DOI: 10.1002/asl.94.
- 7 Viswandapalli, Y., Dasari, H.P., Sanjeev, D., Ratnam, M.V., Langodan S. and Hoteit, I., 2019b:
8 Variability of Monsoon Low Level Jet and associated rainfall over India. *International*
9 *Journal of Climatology*. <https://doi.org/10.1002/joc.6256>.
- 10 Viswanadhapalli, Y., Dasari, H.P., Langodan, Challa S. and Hoteit, I., 2017. Climatic features of
11 the Red Sea from a regional assimilative model. *Int. J. Climatol.* 37, 5, 2563–2581.
- 12 Wahl, T., Haigh, I.D., Nicholls, R.J., Arns, A., Dangendorf, S., Hinkel, J. and Slangen, A.B., 2017.
13 Understanding extreme sea levels for broad-scale coastal impact and adaptation
14 analysis. *Nature communications*, 8(1), pp.1-12.
- 15 Wessel, P., Smith, W.H., Scharroo, R., Luis, J. and Wobbe, F., 2013. Generic mapping tools:
16 improved version released. *Eos, Transactions American Geophysical Union*, 94(45),
17 pp.409-410.
- 18 Woodworth, P.L. and Blackman, D.L., 2004. Evidence for systematic changes in extreme high
19 waters since the mid-1970s. *Journal of Climate*, 17(6), pp.1190-1197.
- 20 Zhai, L., Greenan, B., Thomson, R. and Tinis, S., 2019. Use of oceanic reanalysis to improve
21 estimates of extreme storm surge. *Journal of Atmospheric and Oceanic*
22 *Technology*, 36(11), pp.2205-2219.
- 23 Zuo, H., Balmaseda, M.A., Tietsche, S., Mogensen, K. and Mayer, M., 2019. The ECMWF
24 operational ensemble reanalysis–analysis system for ocean and sea ice: a description of the
25 system and assessment. *Ocean Science*, 15(3).
- 26 Zhan, P., Subramanian, A.C., Yao, F. and Hoteit, I., 2014. Eddies in the Red Sea: A statistical and
27 dynamical study. *Journal of Geophysical Research: Oceans*, 119(6), pp.3909-3925.
- 28

Table 1. Error statistics (σ_s , in cm) of harmonic constituents between model and observation. Station numbers are the same as those shown in Figure 1.

Station No.	Constituent	A_o	ϕ_o	A_m	ϕ_m	$ \Delta z $	σ_s
1	K ₁	3.80	162.00	3.59	151.71	0.70	
	M ₂	11.00	113.00	10.19	114.14	0.84	
	N ₂	3.00	84.00	3.25	87.68	0.32	
	O ₂	2.00	165.00	1.89	159.28	0.22	
	S ₂	3.00	147.00	2.74	136.27	0.60	
	K ₂	1.00	147.00	0.75	136.27	0.30	
	P ₁	1.00	162.00	1.19	151.71	0.27	
2							0.96
	K ₁	4.00	165.00	3.61	152.93	0.89	
	M ₂	12.00	117.00	10.37	116.04	1.64	
	N ₂	4.00	88.00	3.31	89.93	0.70	
	O ₂	2.00	168.00	1.91	160.27	0.28	
	S ₂	3.00	146.00	2.79	138.51	0.43	
	K ₂	1.00	146.00	0.76	138.51	0.27	
3	P ₁	1.00	165.00	1.20	152.93	0.30	
							1.48
	K ₁	4.00	163.00	3.58	151.96	0.84	
	M ₂	12.00	115.00	10.07	114.30	1.94	
	N ₂	4.00	85.00	3.22	87.85	0.80	
	O ₂	2.00	169.00	1.89	159.46	0.34	
	S ₂	3.00	145.00	2.70	136.44	0.52	
4	6	1.00	145.00	0.73	136.44	0.30	
	7	1.00	163.00	1.19	151.96	0.28	
							1.68
	K ₁	3.00	154.00	3.57	151.80	0.59	
	M ₂	11.00	115.00	9.98	113.99	1.04	
	N ₂	3.00	76.00	3.19	87.56	0.65	
	O ₂	2.00	165.00	1.89	159.34	0.22	
5	S ₂	4.00	157.00	2.67	136.13	1.78	
	K ₂	1.00	157.00	0.73	136.13	0.41	
	P ₁	1.00	154.00	1.18	151.80	0.19	
							1.62
	K ₁	4.00	163.00	3.57	151.77	0.86	
	M ₂	12.00	114.00	9.90	113.90	2.10	
	N ₂	4.00	84.00	3.17	87.51	0.86	
5	O ₂	2.00	168.00	1.89	159.31	0.32	
	S ₂	3.00	146.00	2.65	136.04	0.60	
	K ₂	1.00	146.00	0.72	136.04	0.32	
	P ₁	1.00	163.00	1.18	151.77	0.28	
							1.80

Table 2: Correlations analysis between long-term (1985–2015) hourly meteorological variables at the locations shown in Figure 6a and corresponding surge time series at KAEC.

Location	North						KAEC						South					
	Pressure	U wind	V wind	Pressure	U wind	V wind	Pressure	U wind	V wind	Pressure	U wind	V wind	Pressure	U wind	V wind	Pressure	U wind	V wind
KAEC	0.65	−0.12	0.08	0.61	−0.18	0.00	0.65	−0.61	0.79									

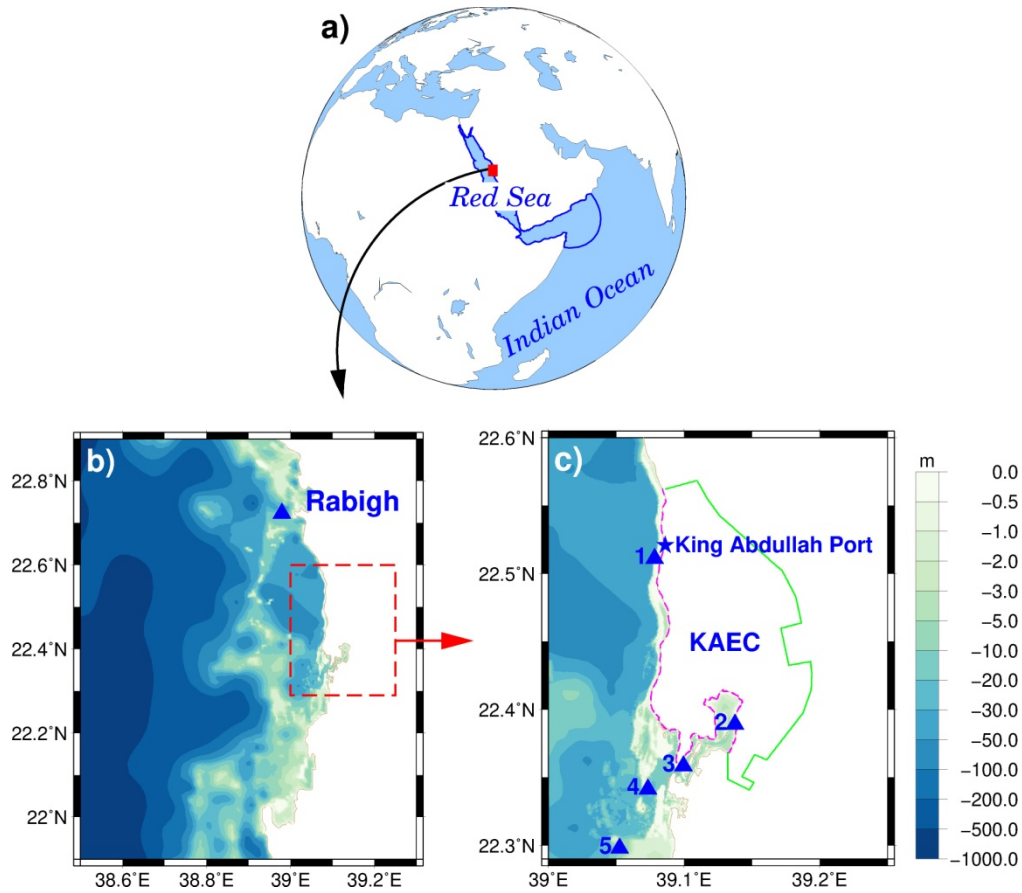


Figure 1. (a) ADCIRC+SWAN model domain is shown on the globe. (b) Location of KAEC and Rabigh tide gauge station. (c) Enlarged image of coastal region surrounding KAEC. Dashed magenta line represents the coastal boundary of KAEC; green line marks the land boundary; triangles show locations of tide data measurement stations.

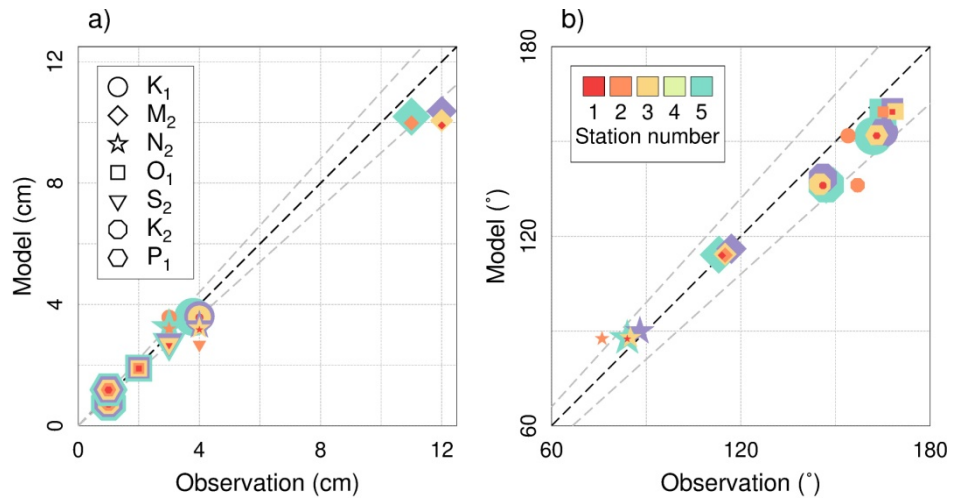


Figure 2. Scatter diagram of (a) amplitudes and (b) phases of observed and modeled tidal constituents. Dashed lines in black and gray represent best agreement and 10% error, respectively.

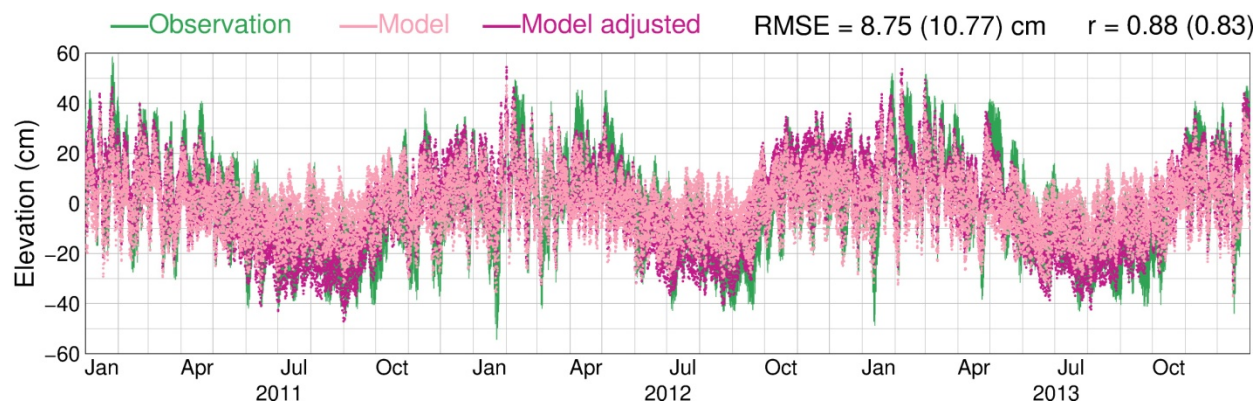


Figure 3. Comparison of observed and modeled water levels at Rabigh. Green line represents observations. Dotted lines in pink and magenta represent 2D model and adjusted 2D model data, respectively. Model validation error statistics for adjusted 2D model and 2D model (in brackets) are provided.

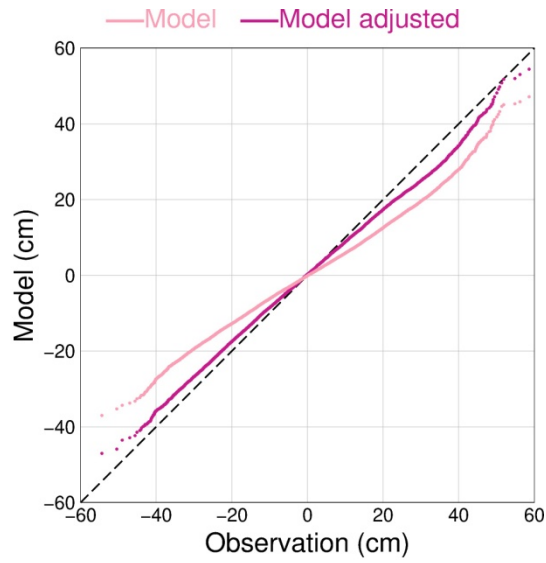


Figure 4. Q-q plot of the modeled water level versus the observed water level at Rabigh. Pink and magenta colors represent 2D model and adjusted 2D model data, respectively. Dashed line in black represents best agreement line.

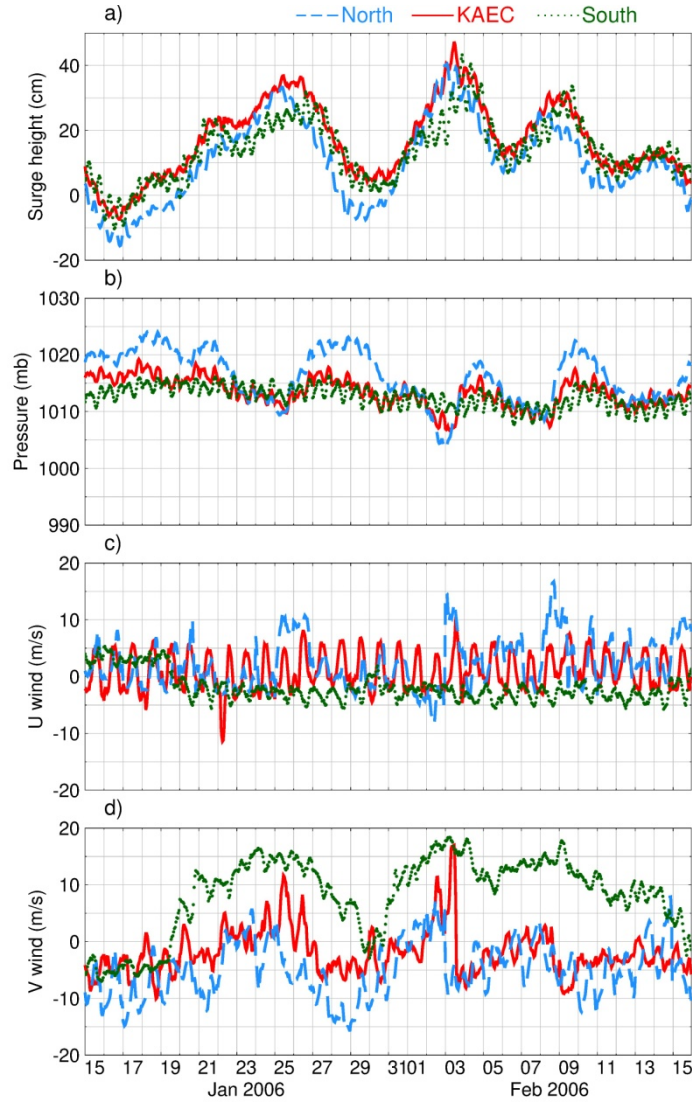


Figure 5. (a) Time series of surge component of water level during January-February 2006 at locations (see Figure 6a for locations) in the northern and southern Red Sea and near KAEC; similarly, those of (b) mean sea level pressure, (c) zonal, and (d) meridional components of surface (10 m) wind speed.

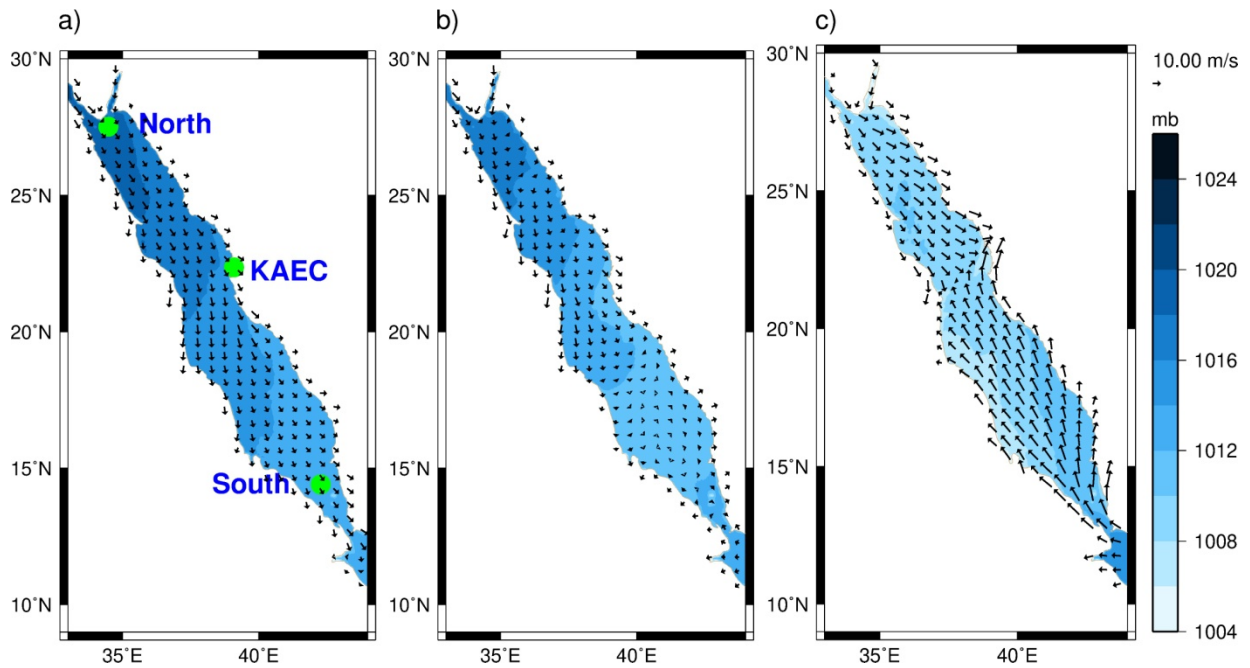


Figure 6. Surface (10 m) wind and mean sea level pressure fields at (a) 11:00 UTC on 16 January 2006, (b) 11:00 UTC on 30 January 2006 and (c) 11:00 UTC on 03 February 2006.

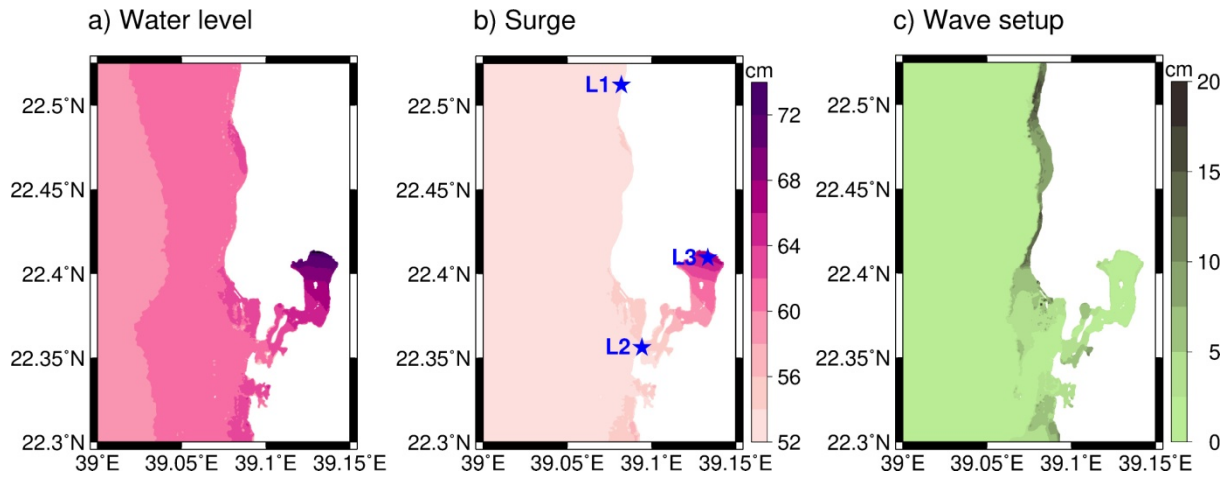
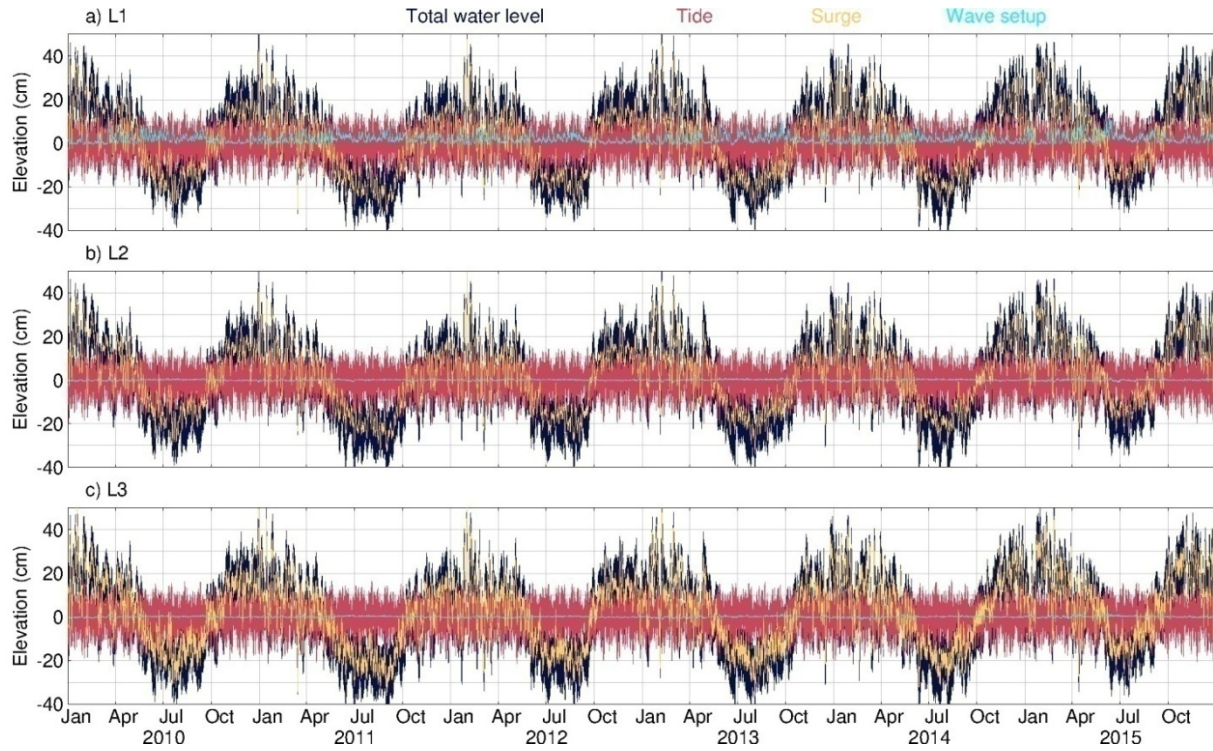


Figure 7. Spatial distribution of maximum (a) water level, (b) surge, and (c) wave setup. Maximum water level and surge are presented with shades of magenta and maximum wave setup is colored with shades of green.

1



2

3 **Figure 8.** Time series of model-simulated tides, meteorological surge, wave setup, and total water
 4 level at three locations (see Figure 7b for locations) in the coastal waters of KAEC. Black, red,
 5 yellow and cyan colors represent total water level, tide, surge and wave setup, respectively.

6

7

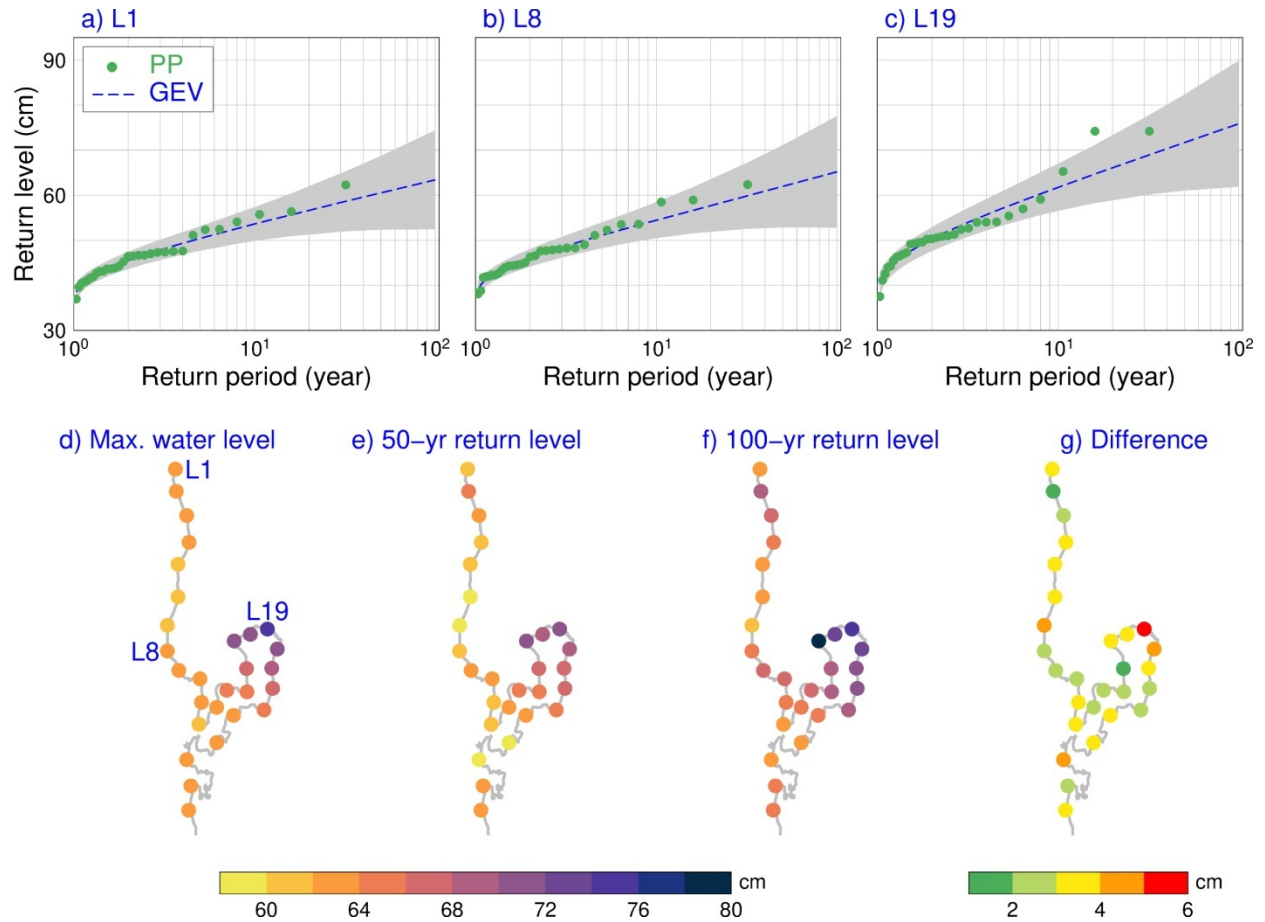
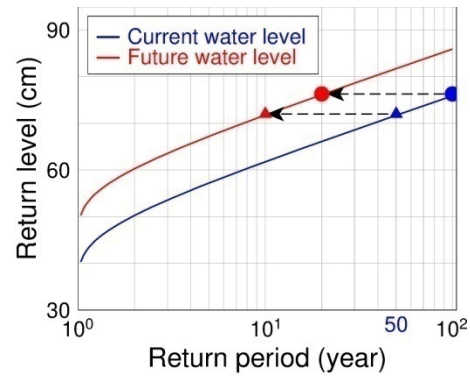


Figure 9. (a–c) Return level curves with 95% confidence intervals (shaded areas) at three selected locations shown in panel (d). Green circles represent plotting positions (PP) of annual maxima and dashed line in blue represents fitted Generalized Extreme Value (GEV) distribution. (d) Maximum water levels during simulation period. (e) and (f) 50- and 100-yr return levels. (h) Difference between 31-yr maximum water level and corresponding return level from extreme value analysis.



1

2

3

4

5

Figure 10. Return period curves at L19 under current climate (blue) and future sea level rise scenario (red). Blue triangle and circle represent 50- and 100-yr return levels under current climate, and red triangle and circle represent positions of current 50- and 100-yr return levels on the future return curve.